

A THESIS SUBMITTED TO THE UNIVERSITY OF MANCHESTER  
FOR THE DEGREE OF DOCTOR OF PHILOSOPHY IN THE FACULTY  
OF SCIENCE AND ENGINEERING

---

# Nuclear Structure Information from Transfer Reactions on Neutrinoless Double Beta Decay Candidate Nuclei

---

*Author:*

Benjamin CROPPER

*Supervisors:*

Professor Sean FREEMAN

Dr David SHARP

Nuclear Physics Group  
Department of Physics and Astronomy  
University of Manchester

May 2021



# Contents

<b>Contents</b>	<b>i</b>
<b>List of Figures</b>	<b>ii</b>
<b>1 Experimental Details</b>	<b>1</b>
1.1 Ion Sources . . . . .	2
1.1.1 Multicusp Source . . . . .	2
1.1.2 Stern-Gerlach Source . . . . .	3
1.2 The Tandem Accelerator . . . . .	4
1.3 Targets . . . . .	6
1.4 The Q3D Spectrograph . . . . .	8
1.5 Focal Plane Detector . . . . .	11
1.6 Signal Processing and Data Acquisition . . . . .	13
1.7 Experimental Considerations . . . . .	16
1.7.1 Momentum Matching . . . . .	16
1.7.2 Angular Distributions . . . . .	17
1.7.3 Target Thickness . . . . .	20
1.7.4 Contaminants . . . . .	22
1.7.5 Magnetic Field Settings . . . . .	23
1.7.6 Resolution Considerations . . . . .	23
<b>Bibliography</b>	<b>26</b>

# List of Figures

1.1	The layout of the Maier-Leibnitz Laboratory . . . . .	2
1.2	Diagram of the multicusp ion source . . . . .	3
1.3	Diagram of the Stern-Gerlach ion source . . . . .	4
1.4	Schematic of a MP tandem Van de Graaff accelerator . . . . .	5
1.5	Sketch of the 90° beam-analysing magnet . . . . .	6
1.6	Photograph of the MLL target ladder . . . . .	7
1.7	Schematic of the Q3D target chamber . . . . .	7
1.8	Schematic of the A aperture entrance to the Q3D Spectrograph . . . . .	8
1.9	Schematic diagram of the Q3D magnetic spectrograph . . . . .	10
1.10	Diagram of the focal plane detector . . . . .	12
1.11	Illustration of the principle of cathode strip detectors . . . . .	13
1.12	Schematic diagram of the Q3D focal plane electronics . . . . .	14
1.13	Angular distributions for $(p, d)$ and $(d, p)$ at different lab energies . . . . .	18
1.14	Angular distributions for $(^3\text{He}, \alpha)$ at different lab energies . . . . .	19
1.15	Fraction of Rutherford cross section for 9 MeV deuteron elastic scattering . . . . .	21
1.16	Example of a light mass contaminant peak . . . . .	22

# Chapter 1

## Experimental Details

The experiments that this work is based on were done at the Q3D spectrograph at the Maier-Leibnitz Laboratorium (MLL) in Munich, and the details of the laboratory and the specifics of these experiments will be discussed in this chapter. A diagram of the layout of the MLL is shown in Figure 1.1 ( $d, p$ ), ( $p, d$ ) and ( $^3\text{He}, \alpha$ ) reactions were done, with  $^{116}\text{Cd}$ ,  $^{114}\text{Cd}$ , and  $^{116}\text{Sn}$  targets.

Beams of protons, deuterons and  $^3\text{He}$  ions were accelerated by the MP Tandem Van de Graaff accelerator at the MLL, to energies of 22 MeV, 15 MeV, and 33 MeV respectively. The beams were directed to be incident on the targets, and the ejectiles were then scattered into the Q3D. Measurements were taken at a range of Q3D angles for each reaction, with angles chosen to facilitate the analysis of angular distributions. The ejectiles were separated by their momentum by the Q3D onto a focal plane detector, where both their position and energy loss characteristics were measured.

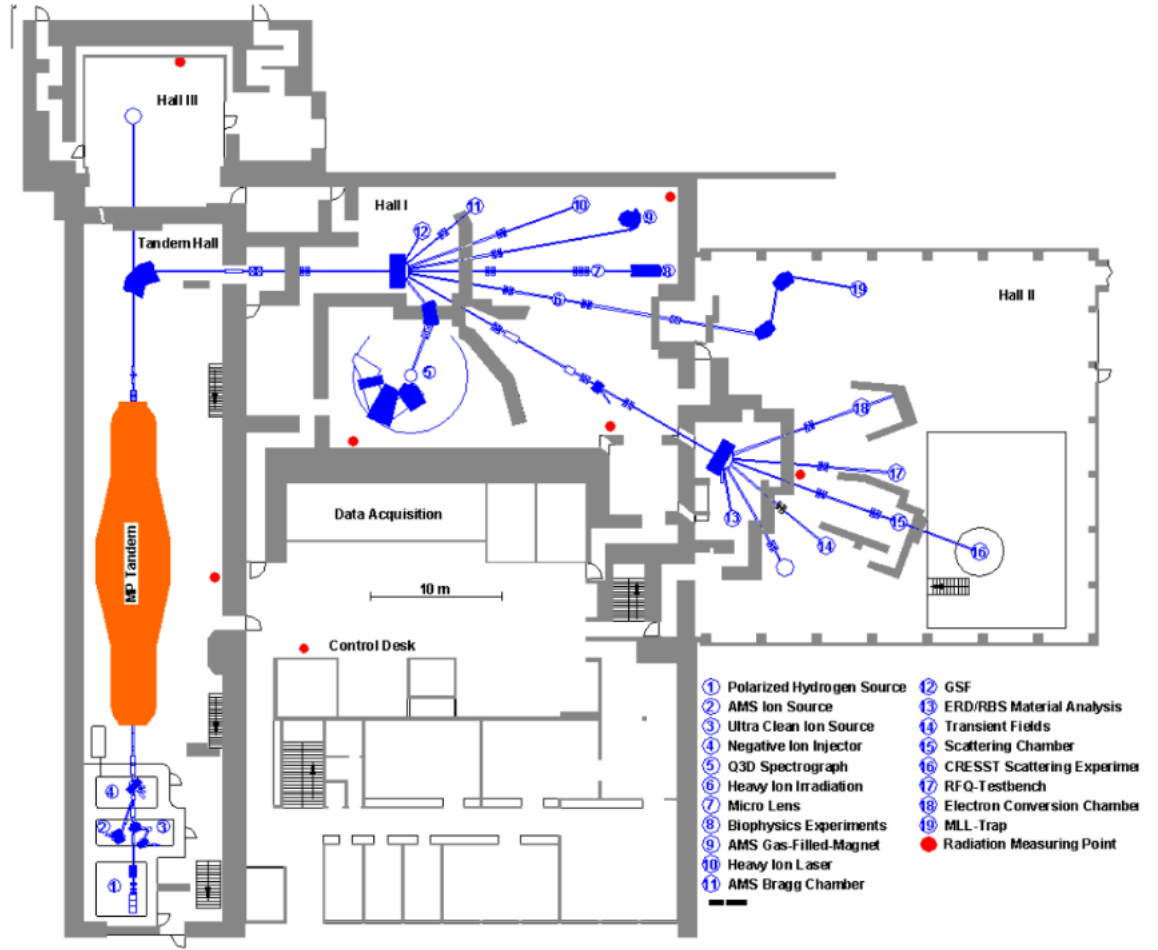


FIGURE 1.1: A diagram which shows the layout of the Maier-Leibnitz Laboratorium, with beam lines and experiments shown in blue. [1]

## 1.1 Ion Sources

The MP Tandem Van de Graaff accelerator at the MLL accepts negative ions to be accelerated, as its central terminal has a positive charge in order to generate the accelerating voltage. There were two ion sources used in these experiments at the MLL to supply the accelerator with negative ions. These were a high-brilliance multicusp source [2], which was used to create the hydrogen beams, and an electron cyclotron resonance (ECR) source [3], which was used to produce the  $^3\text{He}$  beams.

### 1.1.1 Multicusp Source

The multicusp source at the MLL is used to create hydrogen beams with a higher intensity than the other sources [2]. A diagram of this source is shown in Figure 1.2.

The ions are generated in a metallic cylinder in the source. The cylinder is filled with hydrogen gas, which is converted to a plasma by a tungsten filament cathode held at a potential of  $-100\text{ V}$  relative to the anode, with a current of  $50\text{ A}$ . The electrons in this plasma can then collide and attach to neutral hydrogen molecules, which leads to a dissociation of the constituent atoms into a neutral atom and a negative ion. Plasma electrons can also destroy  $\text{H}^-$  ions, but the creation process is favoured at lower electron energies ( $\sim 1\text{ eV}$ ) than produced by the filament, so the energies of the electrons must be reduced in the region where negative ion production takes place [4].

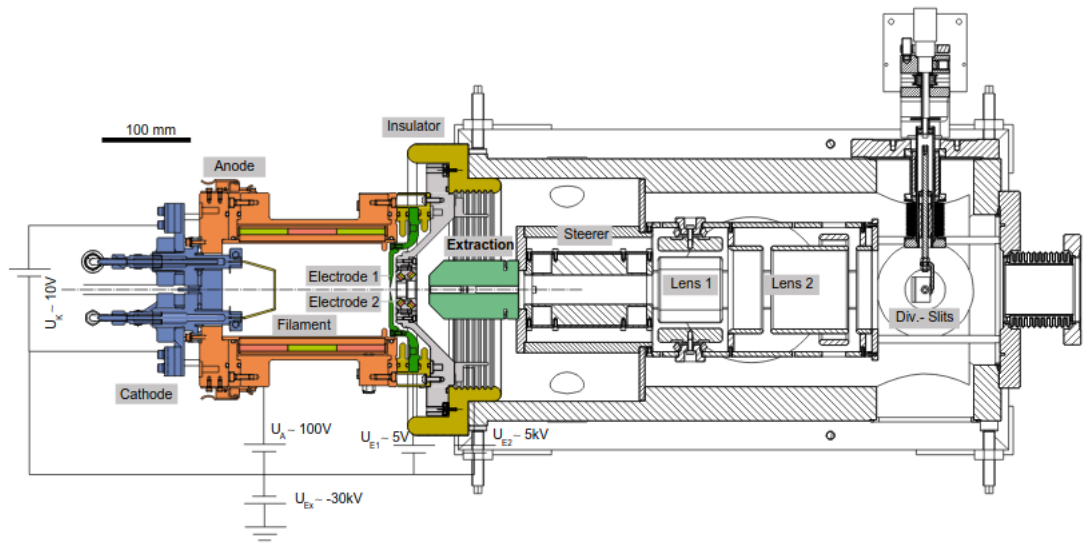


FIGURE 1.2: A diagram of the multicusp ion source used to produce hydrogen beams. The areas shown in colour are the parts of the source that produce the beam of ions, and the grey area is a beam transfer box, which steers the beam, focuses it, and transfers it to the accelerator [2]

### 1.1.2 Stern-Gerlach Source

This was operated without using the polarising Stern-Gerlach magnets, as no polarisation was needed for these measurements. As a result, this ion source acted as an ECR ion source, combined with a charge exchange cell. The charge exchange cell was required because the ECR source produces positive ions, and the accelerator accepts negative ions. A schematic of this source is shown in Figure 1.3

The first part of the ion source is the atomic beam source. This is broken down into four differential pumping stages. By adiabatic expansion into the vacuum in stage one, an atomic jet is formed. The first stage houses a high-frequency circuit which is used to dissociate hydrogen molecules, and the third and fourth stages have hexapole magnets

and adiabatic radio-frequency transitions which are used together to polarise the nuclei. None of these were used in this experiment as unpolarised helium beams were used, so the atomic jet passed directly through the differential pumping into the ECR chamber.

The ECR ion source works by applying a radio-frequency (RF) signal to the beam gas. This is done in a constant magnetic field, so that the RF frequency matched the natural gyro-frequency of electrons in that magnetic field. This causes resonant acceleration in free electrons in the gas, which ionises the gas by colliding the resonant electrons with the gas atoms. These positive ions then pass through a caesium jet in the charge exchange cell, which causes them to pick up two electrons and become negative ions. These are then accelerated to 10 keV and accepted into the accelerator.

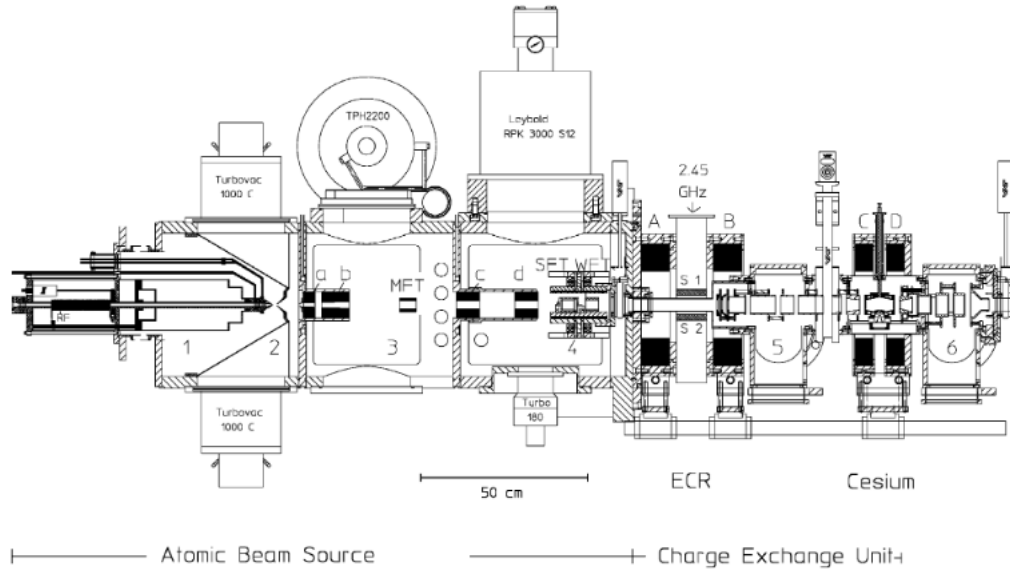


FIGURE 1.3: A schematic of the Stern-Gerlach source at the MLL, used in this work to produce the helium beams. 1, 2, 3, and 4 mark differential pumping stages. [3]

## 1.2 The Tandem Accelerator

The negative ions from the ion source are injected, via a 150 kV potential, into the MP tandem Van de Graaff accelerator. In this work, the ions were accelerated to 15 MeV (deuterons), 22 MeV (protons), and 33 MeV ( $^3\text{He}$ ). A central terminal of the accelerator is charged to a high voltage, which can reach approximately 15 MV [5]. However, in practice it operates at 1 MV below this to decrease instability and risk of electric discharge.

In the evacuated beam line inside the accelerator, negative ions are accelerated towards the central terminal by the electrostatic force. The terminal potential was maintained

using two pelletron chains, which consist of a chain made of metal pellets connected by insulating nylon, rotating on two pulleys [6]. One pulley is at the terminal in the centre of the accelerator, and the other is situated by an inductor at the end of the accelerator close to ground, which charges the pellets. After being charged, they transport positive charge to the terminal, and transport negative charge away on the return journey. A carbon stripper foil is placed in the central terminal, such that the beam ions lose their electrons upon passing through it [7]. The newly positive beam ions are consequently accelerated away from the terminal with the same voltage. The energy of the beam  $E_{\text{beam}}$  is therefore

$$E_{\text{beam}} = (|q_1| + |q_2|)V, \quad (1.1)$$

where  $|q_1|$  and  $|q_2|$  are the magnitude of the charges of the beam ions before and after being stripped of electrons, and  $V$  is the terminal voltage. Equipotential rings surround the central column of the accelerator, which are each held at intervals of increasing voltage, such that the voltage increases slowly and predictably along the accelerator, reducing the risks of sparks. A diagram of the tandem accelerator is shown in Figure 1.4.

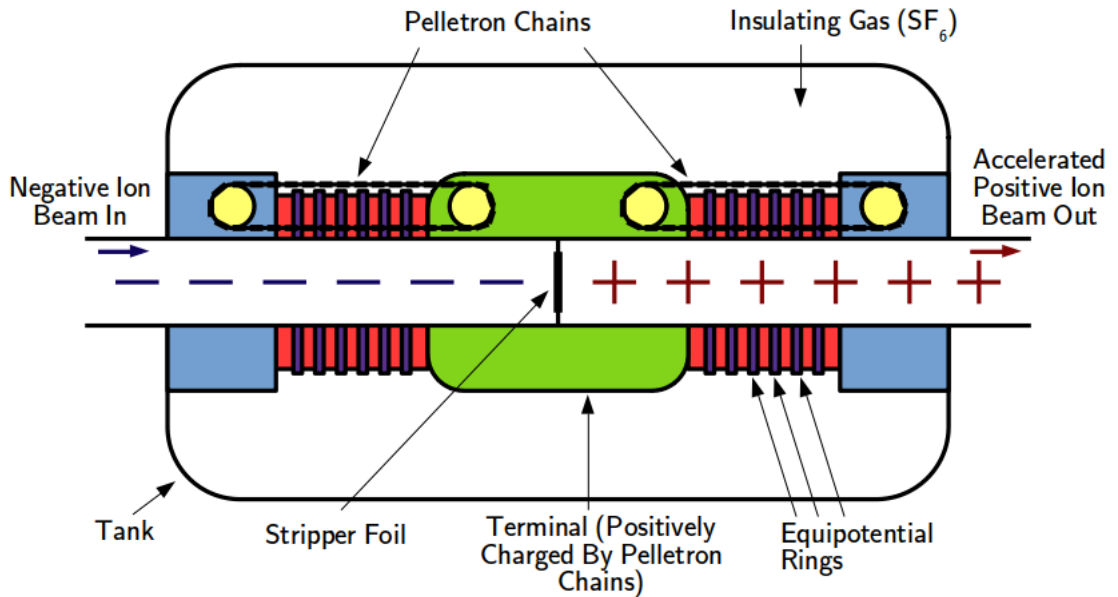


FIGURE 1.4: Schematic of the MP Tandem Van de Graaff generator used at MLL.

In this experiment, the hydrogen beams used had a beam energy equal to  $2V$ , since the beam particles had  $-1$  charge before and  $+1$  charge after passing through the stripper foil. For hydrogen, the voltage was held at 7.5 MV for deuterons, 11 MV for protons and  $^3\text{He}$ , and 4.5 MV for elastic scattering measurements. The  $^3\text{He}$  ions had an energy of  $3V$ , as it has a charge of  $+2$  when stripped of electrons.



After acceleration, the beam passes through a  $90^\circ$  analysing magnet, which is a negative feedback mechanism for preventing beam energy instability due to fluctuations in the voltage. The radius of curvature  $\rho$  of a particle with momentum  $p$ , mass  $m$ , kinetic energy  $E$  and charge  $q$  in a constant magnetic field of strength  $B$  is

$$\rho = \frac{p}{qB} = \frac{\sqrt{2mE}}{qB}. \quad (1.2)$$

For the  $90^\circ$  analysing magnet, the field is set such that the beam, if it has the correct energy, passes through a pair of slits after the bend. If the energy is not correct, the beam does not have the correct radius of curvature and therefore is not incident on the slits. The current on these slits is measured and the accelerator voltage is automatically adjusted accordingly. A sketch of how this operates is shown in Figure 1.5. This keeps the beam energy resolution  $\Delta E/E$  to less than  $3 \times 10^{-4}$  [8], which is a negligible contribution to the overall energy resolution of the experiment.

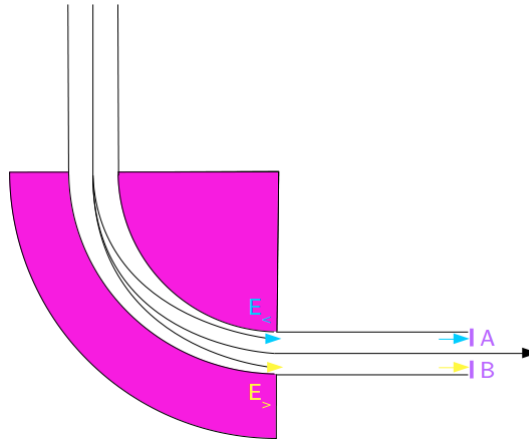


FIGURE 1.5: An illustration on how the analysing magnet rejects ions with too much energy ( $E_{>}$ ) and not enough energy ( $E_{<}$ ). Ions with energy  $E_{>}$  have a bending radius which is too large, and are intercepted by slit B. Conversely, ions with energy  $E_{<}$  have a bending radius which is too small, and are intercepted by slit A.

### 1.3 Targets

Film targets are placed on a target ladder, which can hold up to five targets. There is also another slot on the ladder, which is a collimator used for beam tuning. The target ladders are shown in Figure 1.6, with targets mounted.

For the measurements discussed in this work, targets were all prepared by evaporating the target material onto a carbon backing with a thickness of  $10\text{-}30 \mu\text{g cm}^{-2}$ . Each target

had thicknesses between  $30 \mu\text{g cm}^{-2}$  and  $120 \mu\text{g cm}^{-2}$ . The tin targets used here were oxides, whereas cadmium targets were metallic.

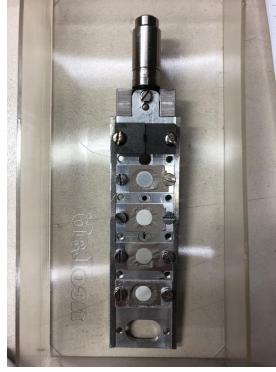


FIGURE 1.6: Photograph of the target ladder, with the mount at the top, followed by a collimator, and then four slits with targets mounted. The bottom slit was empty because the mounting system physically prevented this slot from being moved into the correct position.

The target ladder is situated in a cylindrical target chamber. The chamber can be isolated from the beam line so it can be vented separately, allowing the target ladder to be changed without disturbing the vacuum in the rest of the beam line. There is also a rotating seal, so the spectrograph can be rotated around the target chamber to measure reaction products at different scattering angles. Behind the target, a Faraday cup is positioned, which is connected to a Brookhaven current integrator [9] to measure the charge collected during each measurement. A sketch of the target chamber is shown in Figure 1.7, showing the relative positions of the spectrograph, target ladder, and beam line.

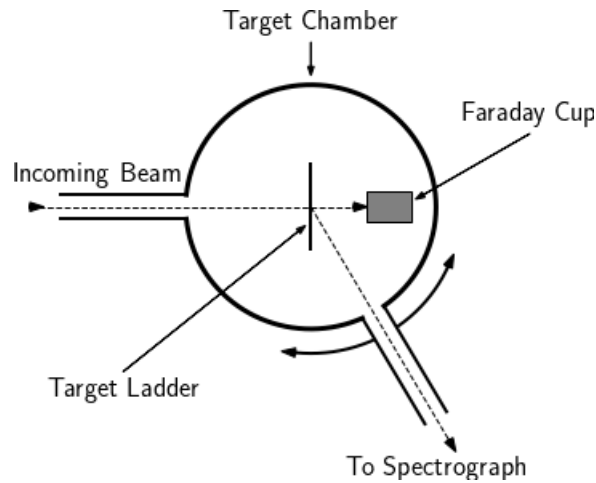


FIGURE 1.7: A schematic diagram of the target chamber. Note that a Faraday cup is placed behind the target to measure the beam current, and that the angle of the spectrograph can be altered.

At the entrance to the spectrometer, there is an aperture, such that the acceptance of the spectrometer could be adjusted. The shape of the aperture is a rhombus with width  $2A = 63$  mm and height  $2B = 73.4$  mm, oriented such that the diagonals are the horizontal and vertical axes. There are horizontal and vertical slits, which are adjustable, opening symmetrically from the centre of the aperture, and they set the angular acceptance of the spectrometer. There is a diagram of the aperture shown in Figure 1.8. The aperture size was set to 14.03 msr, which is a fully open aperture, except for at forward scattering angles with high-intensity hydrogen beams, where it was set to 7.25 msr. This was done to prevent detector saturation due to large elastic scattering cross sections at these angles. A fully-open aperture corresponds to an angular acceptance of  $\sim 3^\circ$ .

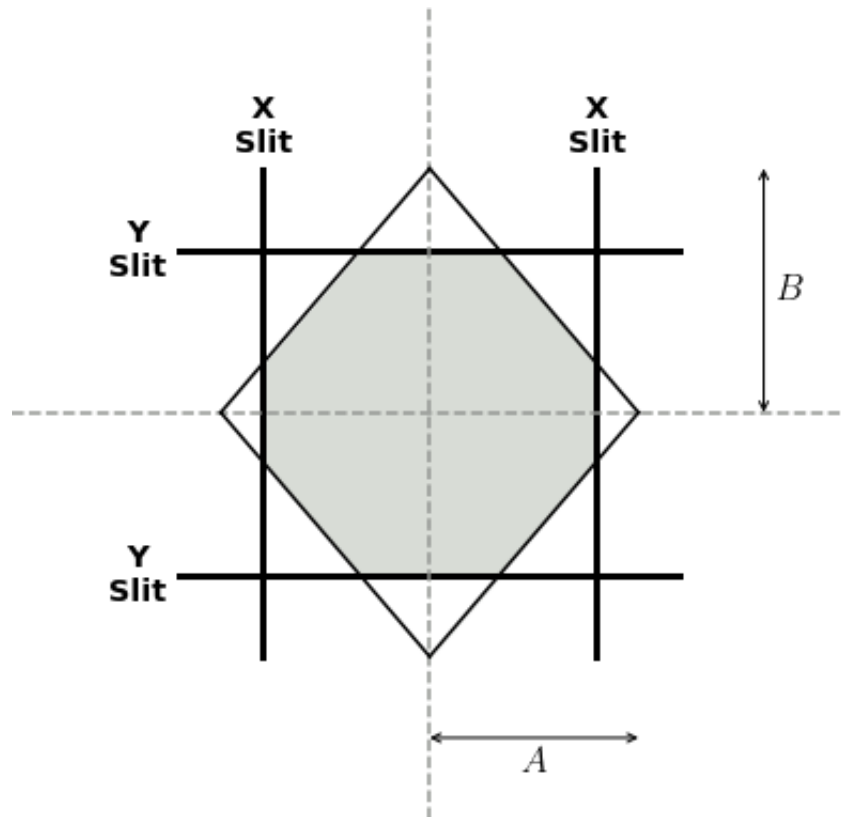


FIGURE 1.8: A schematic of the aperture. The rhombus is the aperture, and the bold lines are the slits that overlap it. The grey area is the effective aperture, which is obscured by neither the slits, nor the aperture itself.

## 1.4 The Q3D Spectrograph

The Q3D spectrograph separates ejectiles dispersively by their momentum. A magnetic field is used to do this, as charged particles of different momenta have different bending radii. The ejectiles are steered onto a focal plane, with their position on the plane

perpendicular to their direction of movement being proportional to their momenta. This position is measured by a focal plane detector.

These momenta are proportional to the square root of their kinetic energy, and their kinetic energy  $E$  is related to the excitation energy of the product nucleus  $E_x$  by

$$E = E_b - E_x - E_p + Q, \quad (1.3)$$

where  $E_b$  is the energy of the beam,  $Q$  is the Q-value of the reaction, and  $E_p$  is the kinetic energy of the product nucleus. As a result of measuring the momenta of the ejectiles, states of different energies in the product nucleus can then be identified and analysed.

To show how we can extract the momenta, we compare the condition for circular motion

$$F = \frac{mv^2}{\rho}, \quad (1.4)$$

where  $F$  is the radial force experienced by the reaction product,  $m$  is the mass of the reaction product,  $v$  is the velocity, and  $\rho$  is the radius of curvature, with the Lorentz equation for a charged particle moving perpendicular to a magnetic field,

$$F = qBv, \quad (1.5)$$

where  $F$  is the magnitude of the force,  $q$  is the charge,  $B$  is the magnetic field strength and  $v$  is the velocity. This results in

$$mv = qB\rho, \quad (1.6)$$

showing that non-relativistic momentum  $p = mv$  is proportional to  $\rho$  in a perpendicular magnetic field.  $B\rho$  is known as the magnetic rigidity. This shows the concept of how the Q3D spectrometer separates ejectiles radially. The magnetic field of the spectrograph is more complex, however, using one quadrupole magnet and three dipole magnets to effect the overall field. Figure 1.9 is a sketch of the spectrograph, showing the configuration of the magnets.

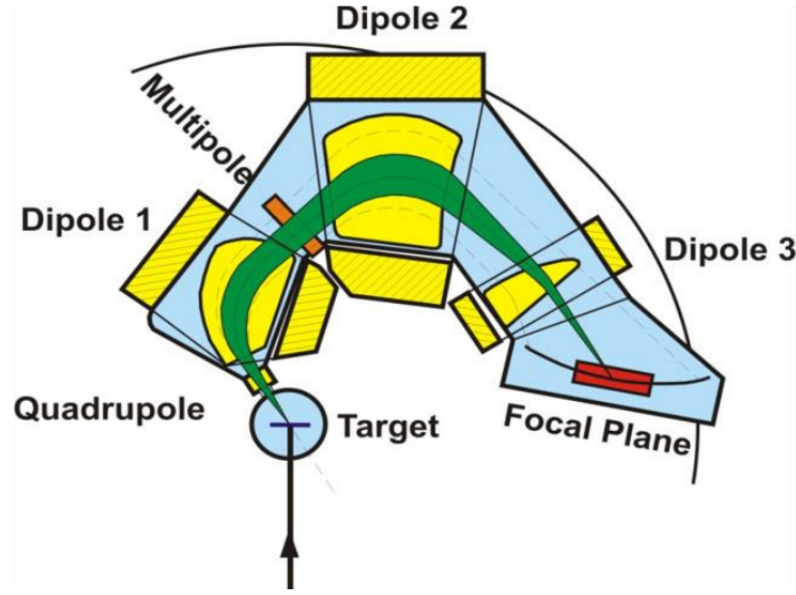


FIGURE 1.9: Sketch of the Q3D spectrograph, showing paths of ejectiles from the target to the focal plane. [10]

While the dipole magnets provided the radial bending, the quadrupole increased the vertical acceptance of the spectrometer by focusing ejectiles into the focal plane of the detector. There was also a multipole element to correct for kinematic broadening [11]. Overall, the ejectiles were vertically focused and bent horizontally into this focal plane, where a detector was placed.

Kinematic broadening is a defocusing effect produced by having a finite aperture. While in the centre-of-mass frame the energy of the scattered ejectile is uniform, in the laboratory frame there is an angular dependence between  $E$  and the scattering angle, as some of the energy is transferred as kinetic energy to the product nucleus. Therefore, particles produced from a reaction to the same state in the product nucleus that go through one side of the  $3^\circ$  aperture have a different energy to particles that get through the other side. They have different bending radii, so the position of particles from that state is spread out more on the focal plane detector, decreasing the resolution. The overall effect of this is a broadening  $k$  of

$$k = \frac{1}{p} \frac{dp}{d\theta}, \quad (1.7)$$

where  $p$  is the momentum of the ejectile and  $\theta$  is the scattering angle.

The reason to separate the ejectiles by their energy is to measure each state in the nucleus separately. It is therefore useful to define a measure of how close in momentum two particles can be and still be resolved, which is a measure of how well a spectrograph can resolve states. This measure is called resolving power, and is given by

$$\frac{\Delta p}{p} = \frac{M_x x_0}{D}, \quad (1.8)$$

where  $x_0$  is the distance between two objects on the focal plane,  $D$  is the dispersion, and  $M_x$  is the magnification. A smaller  $\frac{\Delta p}{p}$  is a higher resolving power. Therefore, for a higher resolving power of these two objects, the spectrometer must have a higher dispersion and lower magnification.

With these, we can characterise a spectrograph. For the Q3D, its specifications are given in Table 1.1. Its dispersion is high, which means that it has a good resolution, however it also means that there is a large physical distance over which reaction products spread on the focal plane. For the  $(d, p)$  and  $(p, d)$  reactions, this spread is larger than the size of the focal plane detector, so the spectra for these reactions must be measured in multiple parts, or "bites", to measure at all of the relevant energies in these spectra.

Characteristic	Symbol	Munich Q3D
Orbital radius	$\rho$	95 to 105 cm
Resolving power	$\frac{\Delta p}{p}$	5000
Maximum horizontal acceptance		55 mrad
Maximum vertical acceptance		63 mrad
Maximum angular acceptance	$\Omega$	14.03 msr
Dispersion	$D$	20 cm \ % momentum bite along focal plane
Focal plane length		2.20 m
Magnetic field		2.7 to 17 kG

TABLE 1.1: The specifications of the Munich Q3D spectrograph [12]

## 1.5 Focal Plane Detector

The focal plane detector has two purposes: to measure the position, and therefore momentum, of the reaction products, and to identify the species of each particle that is incident to make sure that only particles from the correct reaction are used.

The focal plane detector system comprises three detectors. Two are Multi-Wire Proportional Counters (MWPCs) and one was a plastic scintillator. The layout of the detectors

is shown in Figure 1.10, with the MWPCs shown in front of the scintillator. The detector is configured this way so that an incoming particle can have its pattern of energy deposition charted through the detectors: it first deposits some of its energy in the first proportional counter, then some more in the second, and it finally deposits the rest in the thick scintillator, where it stops. The proportion of a particle's energy deposition is characteristic of the species of particle, so this is how the detector identifies the species.

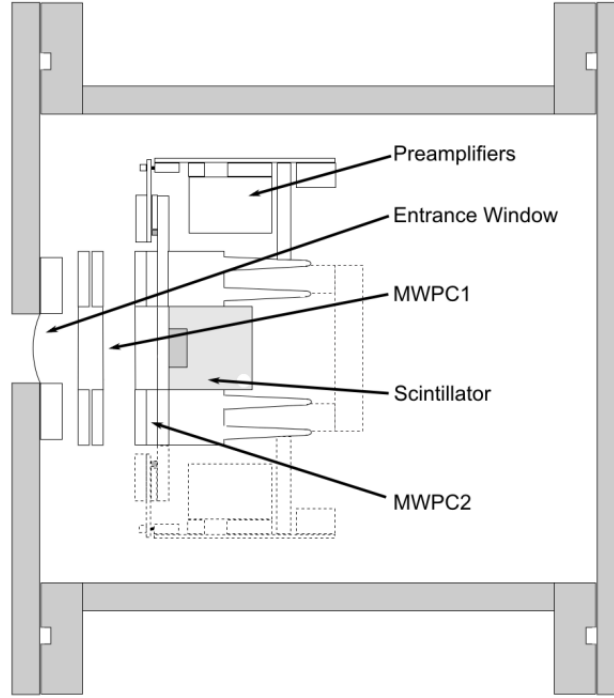


FIGURE 1.10: Diagram of the layout of the focal plane detector [13, 14]. The reaction products enter from the left, pass through the two MWPCs and stop in the scintillator.

An MWPC is a sandwich-like setup of parallel anode wires surrounded by isobutane gas, between two cathode foils. The isobutane gas has a pressure of 500 mbar, and the scintillator is made of NE104 plastic, with a cross sectional area of  $7 \times 14 \text{ mm}^2$  and thickness 7 mm. It is surrounded by a light guide with dimensions  $30 \times 30 \times 1030 \text{ mm}^3$ , which couples the scintillator to a photomultiplier tube on each end. [15]

Upon being struck by a particle, the gas ionises. In regions of higher field near to an anode wire, this creates an avalanche, where electrons produced by the ionisation accelerate towards the anode wire and themselves become capable of ionisation. These electrons gather on an anode wire, while the complementary positive ions gather on the cathode.

On the second of the MWPCs at the Munich Q3D, the cathode foil is split into multiple strips across the focal plane, where the charge accumulated on each can be measured.

This allows the position of the ionisation of the gas across the focal plane to be measured, and with it the position of the impact of the reaction product, which is the first purpose of the detector. An event is defined as consisting of 3-6 adjacent strips registering a signal. The position is determined by fitting the collected charge on these strips with a Gaussian function. This process of determining the position is illustrated in Figure 1.11. Note that the cathode strips are equally spaced along the focal plane.

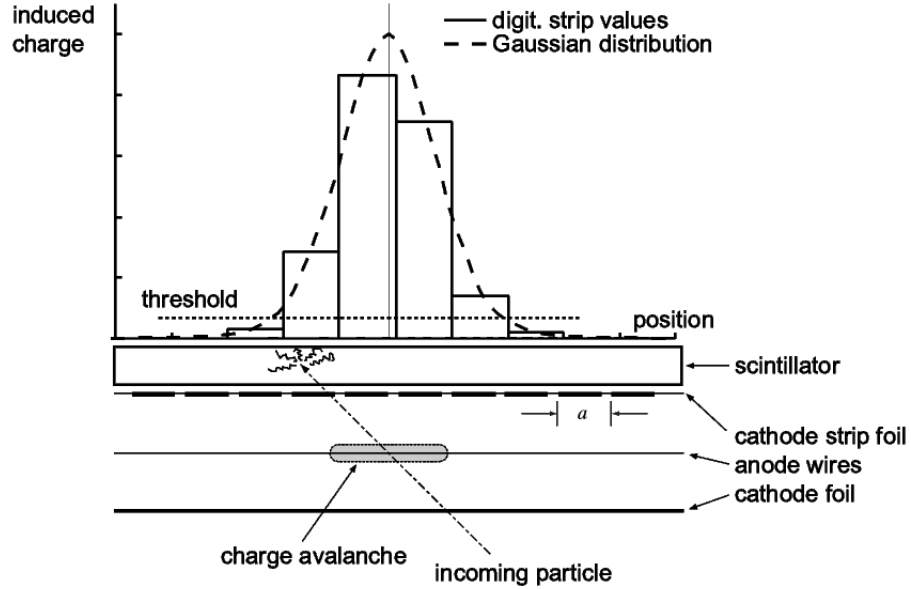


FIGURE 1.11: Illustration of the principle of the cathode strip method of focal plane position determination [14].  $a$  is the repetition distance between cathode strips. A Gaussian distribution was fit to all of the cathode signals which exceed the threshold.

Behind the two MWPCs, the plastic scintillator absorbs the rest of the energy of incoming reaction products. A scintillation detector works by converting the energy of an incoming particle into light, where the number of photons is proportional to the energy deposited by the particle. This light strikes a photocathode, which emits electrons via the photoelectric effect. The electrons are then multiplied in a photomultiplier tube, so the current is proportional to the energy deposited by the original incoming particle. This is then passed through a resistor, so the voltage across the resistor is then proportional to the energy of the initial reaction product [16].

## 1.6 Signal Processing and Data Acquisition

The raw signals from the detectors must then be electronically processed such that they can be interpreted by data-acquisition software and saved into ROOT files and subsequently analysed. It does this by processing signals from the cathode strips, anode wires,



and photomultipliers that in coincidence, constitute an event. A schematic diagram of the electronics is shown in Fig 1.12.

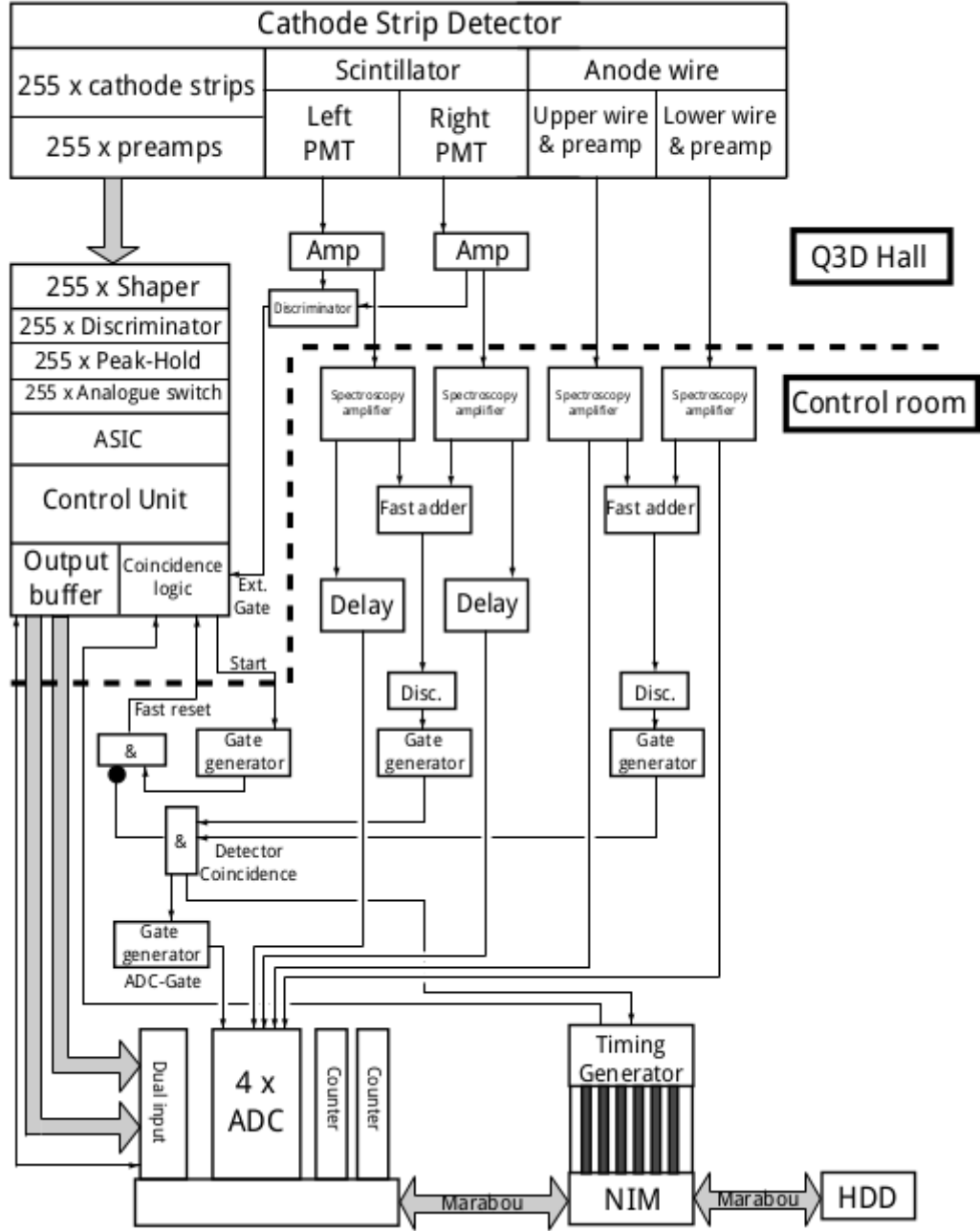


FIGURE 1.12: A schematic diagram of the electronics which process signals from the focal plane detector. Figure taken from [1], which is itself an English-language adaptation from a figure from [15]. A more complete discussion of the electronics can also be found in Ref. [15].

There are 255 cathode strips on the cathode strip detector, and the signals from each pass through preamplifiers and shaping amplifiers. If the signal is large enough, a discriminator is triggered which sends a digital pulse to be processed by an Application Specific Integrated Circuit (ASIC), which deems a signal valid if there are simultaneous signals from three neighbouring strips, i.e. there is a multiplicity of at least three. Meanwhile, the heights of the pulses are recorded in capacitors, such that the position of the signal can be accurately measured (see Figure 1.11).

The ASIC is only active when signals from the photomultipliers are sent and exceed a discriminator threshold. The signal from this discriminator is called the "external gate", and is designed to reduce the load on the ASIC. As well as this, there is a 'fast reset' signal which is generated when the ASIC detects a signal with correct multiplicity but there is no corresponding signal from the anodes or photomultipliers, which allows the ASIC to restart recording promptly after such an event happens. On the other hand, if there is a coincidence in the photomultipliers and the anodes but the ASIC is busy dealing with a previous event, then the data acquisition software (DAQ) is triggered without a signal from the ASIC. In this case, the event is placed into channel zero on the final position spectrum, and this can be used to correct for the dead time of the ASIC. We can define an efficiency  $\varepsilon$  such that

$$\varepsilon = 1 - \frac{P_0}{P_{tot}}, \quad (1.9)$$

where  $P_0$  is the number of counts in channel zero, and  $P_{tot}$  is the total number of counts in the spectrum.

In short, an event is deemed valid if there is a multiplicity of at least three from the cathodes, and there is a coincident signal from the photomultipliers. When this happens, the data is sorted by a control unit and passed to a dual-input register, which is then read by the DAQ. The data acquisition software is called "MARaBOU" (MBS And ROOT Based Online/Offline Utility), where MBS is a C-based data acquisition system made by the GSI laboratory, and ROOT is the data analysis framework made by CERN.

There is one more important consideration when talking about the data acquisition, and that is the correction for the dead time of the DAQ. There are two numbers used to make this correction: Scaler 1 and Scaler 3. Scaler 1 is connected to the BCI (Brookhaven Current Integrator), which measures the beam current and integrates it to give the number of particles in the beam over the course of a measurement. When the DAQ is dealing with an event and cannot accept more events, Scaler 3 also is connected to the BCI. Therefore, the difference between Scaler 1 and Scaler 3 gives the number of

particles in the beam corrected for the dead time of the DAQ, and this number is known as the BIC (Brookhaven Integrated Current).

## 1.7 Experimental Considerations

### 1.7.1 Momentum Matching

For  $^{116}\text{Cd}$ ,  $^{114}\text{Cd}$ , and  $^{116}\text{Sn}$ , the states populated were in between the  $N = 50, 82$  shell closures. This region corresponds to the  $3s, 2d, 1h_{11/2}$ , and  $1g_{7/2}$  orbitals. Some population of the states in the above shell (for addition reactions) and below (for removal reactions) may also be expected.

The  $(p, d)$  and  $(d, p)$  reactions favour population of states with low angular momentum.

The  $Q$  value of a reaction is the difference in rest mass energies of the initial and final states [17]. The deuteron is weakly bound, so the  $Q$  value for  $(p, d)$  and  $(d, p)$  reactions are low, especially on heavy targets where the binding energy per nucleon does not change much as  $A$  changes, which is true for the nuclides considered in this work. In contrast, the alpha particle is very strongly bound [17] compared to nearby nuclides in the Segrè chart, so transfer reactions where the ejectiles are alpha particles often have high  $Q$  values.

For a two body reaction with a moving projectile, and both target and recoil nuclei being stationary,

$$Q = \frac{p_i^2}{2m_i} - \frac{p_f^2}{2m_f}, \quad (1.10)$$

where  $p_i$  and  $m_i$  are the linear momentum and mass of the projectile, and  $p_f$  and  $m_f$  are the linear momentum and mass of the ejectile. The magnitude of the linear momentum transfer is

$$q = |\mathbf{p}_i - \mathbf{p}_f|, \quad (1.11)$$

so for a larger  $Q$ ,  $q$  must also be larger. To show that the angular momentum transfer  $\Delta\ell$  depends on  $q$  and therefore on  $Q$ , we consider the classical expression for angular momentum

$$\mathbf{L} = \mathbf{r} \times \mathbf{p}, \quad (1.12)$$

where  $\mathbf{r}$  is the position relative to the centre of rotation. In a direct reaction,  $\mathbf{r}$  is approximately  $\mathbf{R}$ , the nuclear radius. This is because a direct reaction, by definition, is a reaction with only one interaction between the initial and final states. If  $\mathbf{r}$  is much smaller than  $\mathbf{R}$ , then the projectile has enough overlap with the nucleus for more than one interaction to be likely, and if  $\mathbf{r}$  is larger than  $\mathbf{R}$ , then any interaction with the nucleus is unlikely. So applying this to Equation 1.12, and taking the maximum amount of transferred momentum, we get

$$\Delta\ell = Rq. \quad (1.13)$$

Overall, maximum transferred angular momentum is proportional to the transferred linear momentum, which increases as  $Q$  increases.

This semiclassical picture can also describe the relationship between the scattering angle,  $\delta\ell$  and the beam energy  $E_{\text{lab}}$ . Expanding on Equation 1.11,

$$q = \sqrt{p_i^2 + p_f^2 - 2p_i p_f \cos \theta}, \quad (1.14)$$

where  $\theta$  is the scattering angle. Because  $R$  is constant, it can be seen that  $\delta\ell$  can be increased by increasing the scattering angle.

Conversely, the scattering angle can be reduced by increasing  $E_{\text{lab}}$ . For a given  $q$ , if the lab energy (and therefore  $p_i$ ) increases, the scattering angle becomes smaller. This is because  $p_i^2 + p_f^2$  grows slightly faster than  $2p_i p_f$  with increasing  $p_i$ , so  $\cos \theta$  must get larger to compensate, decreasing  $\theta$ .

This means that angular distributions for all of the possible populated states become forward peaked at high energies.

### 1.7.2 Angular Distributions

The angle and energy dependence of  $\delta\ell$  persist in the quantum picture, as shown by this DWBA model of the  $(d, p)$  and  $(p, d)$  reactions at different energies in Figure 1.13.

At low energies, the cross sections for all values of  $\ell$  are low, and the peaks of the distributions are generally at backward angles. As the energy increases, the cross sections increase and the peaks of the distributions come forward in angle. The distributions of different  $\ell$  peak at different and distinct angles, such that the shape of the distributions are characteristic of each  $\ell$ . As the energy increases further, the distributions all become

forward peaked, making it difficult to distinguish between angular momenta based on the angular distributions alone. Moreover, the cross sections for low- $\ell$  states actually reduce, as states of larger  $\ell$  become better matched to the reaction.

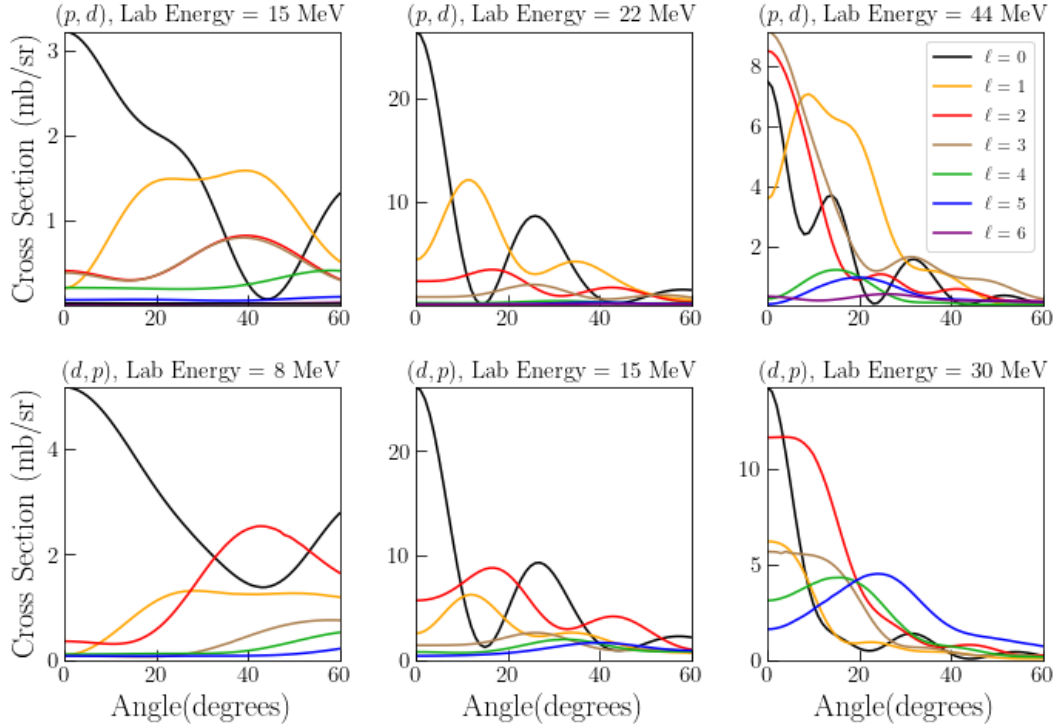


FIGURE 1.13: Angular distributions for  $(p, d)$  and  $(d, p)$  reactions on  $^{116}\text{Cd}$ . These are to the ground state in the daughter nucleus.

These effects were considered when selecting the angles and energies to measure at. 22 MeV was chosen for all  $(p, d)$  reactions and 15 MeV was chosen for  $(d, p)$ . This was such that the peaks of different angular momentum states were distinct, and the cross sections were sufficiently high. The angles where the  $\ell = 0, 2, 4, 5$  distributions peaked were chosen for the measuring angles. The angular momentum of each state was thus deduced by looking at which angle the peak lay.

These angles were  $\theta = (10, 18, 31, 40)^\circ$  for  $(d, p)$ , and  $\theta = (8, 17, 31, 39)^\circ$  for  $(p, d)$ . An additional angle which lay at the peak of the  $\ell = 3$  distribution ( $\theta = 25^\circ$  for  $(d, p)$ ,  $\theta = 26^\circ$  for  $(p, d)$ ) was also measured with a smaller amount of beam time to distinguish between  $\ell = 1$  and  $\ell = 3$  states. The additional angle also ameliorated the obscuring effect of contaminants.

The story for the high- $Q$   $(^3\text{He}, \alpha)$  reaction is slightly different. For this reaction, angular momenta are matched at large energies, and angular distributions are more forward peaked and have fewer distinguishing features between different values of  $\ell$ . This is

shown in Figure 1.14, where as the beam energy increases, the cross sections increase, but the angular distributions are largely featureless at all energies. As a result, it is difficult to assign angular momenta based on the angular distribution alone. The angles taken were  $\theta = (10, 15, 20)^\circ$ . The cross sections become larger if the beam energy is increased further than the 33 MeV used in the experiment, which would be desirable, but this was the largest energy achievable by this spectrograph.

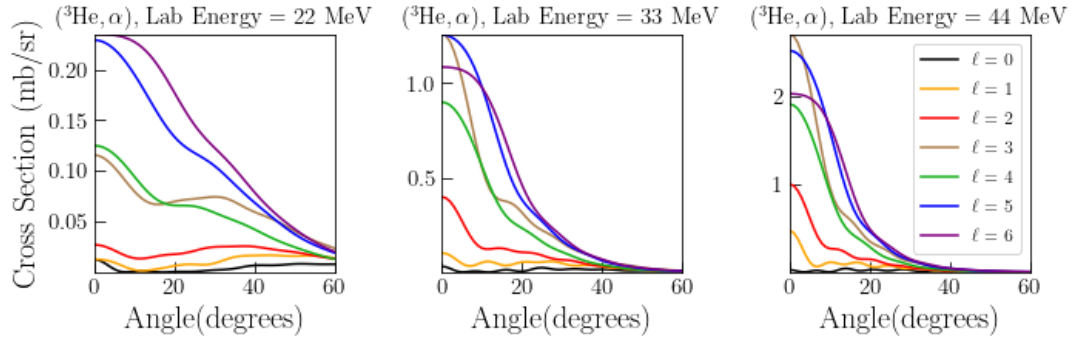


FIGURE 1.14: Angular distributions for  $(^3\text{He}, \alpha)$  reactions on  $^{116}\text{Cd}$ . These are once again to the ground state in the daughter nucleus. The distributions here are have fewer features than the low- $Q$  reactions.

Another way to identify the angular momenta of states is to take the ratio of the cross sections of each state between the  $(p, d)$  and the  $(^3\text{He}, \alpha)$  reactions. States with high  $\ell$  have larger cross sections for the  $(^3\text{He}, \alpha)$  reaction, while the opposite is true for low- $\ell$  states. This ratio, then, tells whether a state has a high or low value of  $\ell$ .

The DWBA code PTOLEMY [18] was used to calculate angular distributions. This code does exact finite range calculations of reaction cross sections, and can produce an angular distribution if provided an angle range and step to do this for. It requires optical-model parameters that describe the entrance and exit channels of the reaction, and some parameters that describe the bound-state wavefunctions of the projectile and target.

It was this that was used to evaluate which angles and energies were best to perform each reaction at. DWBA assumes a single-step direct reaction, so another use of using this method is that it ensures large contributions of this kind of process to the measured cross sections.

Spectroscopic factors are extracted by taking the ratio of measured cross sections to cross sections obtained from DWBA calculations. The DWBA is more accurate when most of the contribution to the cross section is through single step processes, which is at the peaks of the distributions where the DWBA cross section is largest. As a result,

the spectroscopic factors discussed in this work were extracted by taking the ratio at the peaks of the distributions. For the ( $^3\text{He}, \alpha$ ), this was always the furthest forward angle,  $10^\circ$ .

### 1.7.3 Target Thickness

The thickness of the targets were an important consideration, because to extract a cross section of a particular reaction, the number of particles in the target that the beam may interact with must be known.

The reaction yield is related to the differential cross section of that reaction by

$$\frac{d\sigma}{d\Omega} = \frac{Y}{\#t\#b\Delta\Omega\varepsilon p}, \quad (1.15)$$

where  $Y$  is the reaction yield,  $\frac{d\sigma}{d\Omega}$  is the differential cross section,  $\#t$  is the column number density of particles in the target along the beam axis,  $\#b$  is the total number of particles in the beam over the course of the measurement,  $\Delta\Omega$  is the solid angle of the detector aperture,  $\varepsilon$  is the efficiency defined in Equation 1.9, and  $p$  is the isotopic purity of the target.

The target thickness is the area density of the target, which is related to  $\#t$  by

$$\text{target thickness} = m_t\#t, \quad (1.16)$$

where  $m_t$  is the mass of one atom of target material. Target thicknesses are quoted because they are more convenient to write down, but in cross section calculations  $\#t$  is the important number.

When extracting cross sections, the target thickness must be known. To acquire the target thickness, this can be done in reverse: using a reaction with a known cross section to extract the target thickness. The reaction used was elastic scattering, with the Rutherford cross section used to calculate the target thicknesses.

Rutherford scattering is the scattering of charged particles by the Coulomb field of the nucleus. The differential cross section for Rutherford scattering in  $\text{mb sr}^{-1}$  is given by

$$\frac{d\sigma}{d\Omega} = 1.296 \left( \frac{Z_b Z_t}{E_{\text{lab}}} \right)^2 \frac{1}{\sin^4 \frac{\theta}{2}} \quad (1.17)$$

where  $Z_b$  and  $Z_t$  are the proton numbers of the beam and target respectively,  $E_{\text{lab}}$  is the beam energy, and  $\theta$  is the scattering angle [19, 20].

A beam energy and angle are selected such that the Rutherford cross section are a valid approximation of the actual cross section. This is best done at low energies so that the projectiles are less likely to get too close to the nucleus to assume pure Coulomb scattering. The chosen scattering angle can not be small because of the large scattering cross section at these angles, which would swamp the detector. For 9 MeV deuterons at a  $20^\circ$  scattering angle, which was the configuration used for target thickness measurements in the experiments discussed in this thesis, it can be seen in Fig 1.15 that the elastic scattering cross section differed by 2% from the Rutherford cross section.

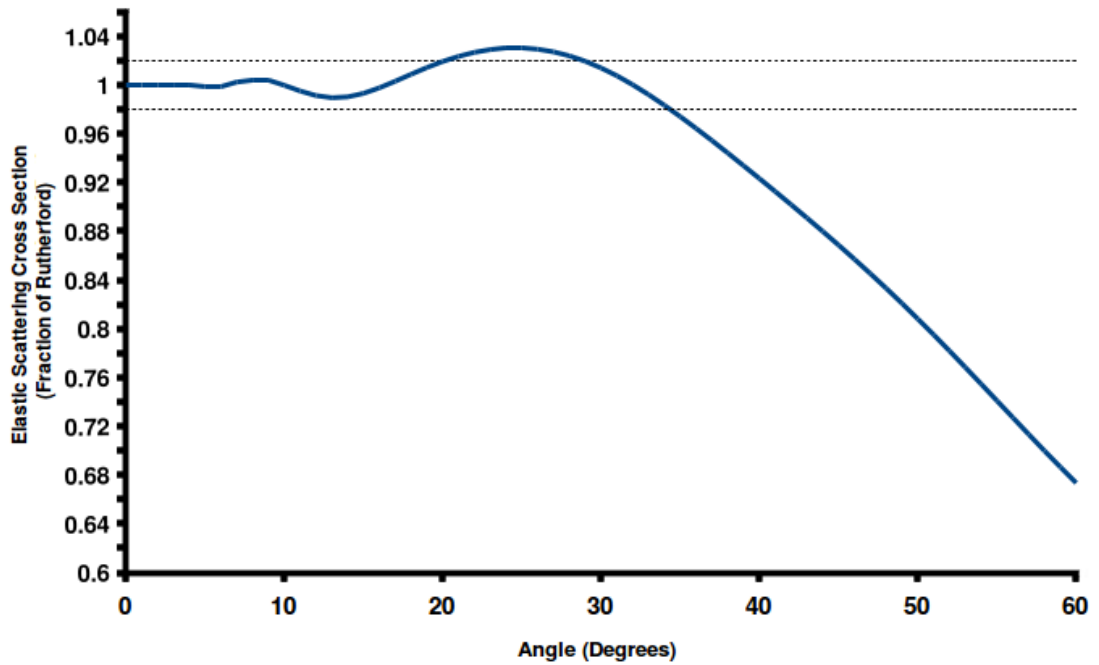


FIGURE 1.15: Fraction of Rutherford cross section for 9 MeV deuteron elastic scattering. The dotted lines mark where the deviation from the Rutherford cross section is 2%. At 20 degrees, the deviation is approximately 2%.

Substituting the Rutherford cross section into Equation 1.15, extracting the yield for this reaction, and finding the other measurement-specific variables gives the target thickness. More specifically, it gives  $\#t\Delta\Omega$ , as the same aperture is used when taking transfer measurements, which means that there is not an extra systematic error coming from a separate measurement of the aperture. This number is then applied when using Equation 1.15 to extract transfer cross sections.



### 1.7.4 Contaminants

In a perfect world, the beam and the target for a transfer experiment would both be completely pure, producing spectra untainted by any other reactions. We can select specific reaction product species from their energy loss characteristics, but we cannot select what those reaction products actually interact with in the target chamber. If there are contaminants in the target, and if the matching reaction emits products with the right rigidities to reach the focal plane, then those reactions cannot be filtered out by the Q3D and they are seen in the final spectra.

There were multiple sources of contamination in the targets that were used in this work that can be seen in the resulting spectra. The tin targets were oxides, so oxygen was present in these spectra, but it could also be seen in the cadmium spectra, possibly because the targets had oxidised upon exposure to the air. The targets were carbon backed, so carbon was also present in the spectra. These could only be seen in the  $(d, p)$  because for other reactions, they fell outside of the focal plane.  $^{14}\text{N}$  was also visible in the  $^{116}\text{Cd}(p, d)$ . Finally, as the targets were not isotopically pure, isotopic contaminants were also present.

The effect of light mass contaminants is the presence of large, broad peaks in the spectra. They are large because the states populated from reactions on  $^{16}\text{O}$  and  $^{12}\text{C}$  had large cross sections from the reaction. The peaks were broad because they were out of focus, as the field was set to focus the ejectiles for reactions on the targets of interests which had a smaller kinematic shift. An example of a light-mass contaminant peak is shown in Fig 1.16.

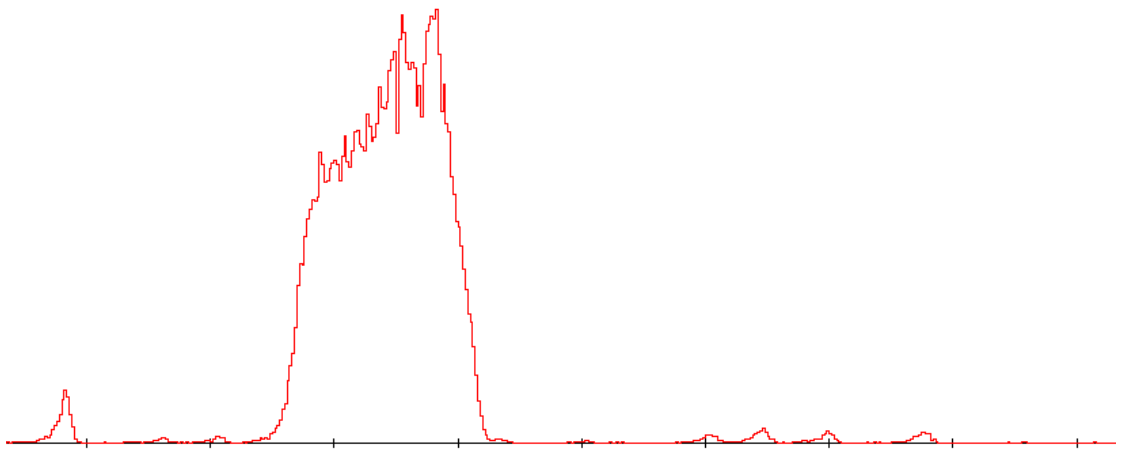


FIGURE 1.16: Example of a light mass contaminant peak. This is in the  $^{116}\text{Sn}(d, p)$  spectrum at a  $30^\circ$  scattering angle. The contaminant peak obscures states at approximately 2.5 MeV. This is the  $^{12}\text{C}(d, p)^{13}\text{C}$  reaction, where the  $^{13}\text{C}$  is in its ground state.

These light-mass contaminant peaks moved along the focal plane at different angle measurements, because of the kinematics of having two particles in collision with comparable masses. This meant that no state was obscured by the contaminant at every angle, but conversely it meant that more states were affected overall. The obscuring effect of the contaminant peaks was also ameliorated by taking the bonus additional measurement.

As well as light mass contaminants, isotopic contaminants were present in the targets, because the enriching process did not fully erase the presence of other natural isotopes. Because each significant isotopic contaminant is at approximately 1% enrichment, strong isotopic contaminant peaks appear with approximately 1% of the yield of strong peaks for the desired reaction. This means they were visible, but at the limit of what could be seen, with less than 100 counts in the peaks. They were identifiable by a  $qB\rho$  calibration of the spectra.

### 1.7.5 Magnetic Field Settings

The nuclear states were probed up to approximately 4 MeV. For the  $(d, p)$  and  $(p, d)$  reactions, this was not possible with one magnetic field setting of the Q3D, because the large dispersion of the Q3D. This meant that states of different energy were separated more along the focal plane, and in this case so much that the 0-4 MeV range was not covered by the focal plane detector. In fact, the energy range covered by one measurement was approximately 1 MeV.

This meant that multiple magnetic field settings had to be used. For  $(d, p)$ , three field settings were used for each target at each angle, while for  $(p, d)$ , four were used. It was ensured that there was an overlap of states between these measurements to allow for an accurate energy calibration.

### 1.7.6 Resolution Considerations

The detector resolution is an important limit of the quality of the data. The resolution is the full width at half maximum (FWHM) of the peaks in the spectra, although it is when this is smaller that the resolution is referred to as greater, because it is a measure of how easy it is to differentiate, or resolve, the peaks. It depends on the physical spread along the focal plane from ejectiles that are from a particular interaction that should all have the same energy. The detector resolution is the part of this which is caused by the configuration of the detector, rather than the intrinsic width of the states involved, and this is always the dominant effect in this work. There are several contributions to this resolution from different physical effects, and these will be discussed in this section.

Some contributions come from effects related to the properties of the target. For example, the position of an interaction across the width of the target has an effect on the scattering angle that the ejectile needs to enter the aperture, increasing the kinematic broadening from the dependence on ejectile energy on the scattering angle in the laboratory frame, which decreases the resolution.

There are also some effects that come from the thickness of the target. Once the reaction has occurred, the ejectile must pass through the target, depositing energy in the target as it does so. The amount of energy it deposits depends on where in the target the reaction occurs. If the reaction happens towards the front of the target from the beam's perspective, the ejectile has more of the target to pass through and thus deposits more energy, and if the reaction happens at the back of the target, the opposite happens. This variability in the energy of the ejectiles contributes to the energy resolution. Using a thinner target ameliorates this issue, but this reduces the reaction yield. Variations in thickness across the beam spot exacerbate this problem.

This energy loss in the target is statistical, as it depends on the number of interactions the ejectile has with matter in the target. Even if two identical reactions happen in the same place in the target, there is some spread in the ejectile energy at the aperture because there is variation in this number of interactions, because these interactions are a random process. This spread also contributes to the energy resolution, and the effect is known as straggling [21].

Variations in energy of the beam are one part in  $10^4$  as discussed in Section 1.2, which is a negligible contribution to the resolution.

These contributions are then compounded by the dispersion of the spectrometer. The dispersion is related to the energy resolution by

$$\Delta x = D \left( \frac{\Delta E}{2E} \right) \rho, \quad (1.18)$$

where  $\Delta x$  is the position resolution on the focal plane,  $D$  is the dispersion,  $\Delta E$  is the energy resolution, and  $E$  and  $\rho$  are the energy and radius of curvature of the incoming particle.

There are two important pieces of information in here. The first is that given a fixed position resolution, spectrometers with a larger dispersion have a greater energy resolution. The Q3D has a comparatively high dispersion, [22] so its resolution is good compared to, say, a split-pole spectrometer.

The second is that the resolution gets worse the higher the ejectile energy gets, which itself depends on the beam energy. The beam energy is just over twice as high for the  $(^3\text{He}, \alpha)$  reaction as it is for the  $(d, p)$  reaction, so the FWHM of the peaks is just over twice as large. Thankfully, the  $(p, d)$  reactions probe the same states as the  $(^3\text{He}, \alpha)$ , revealing the structure of unresolved multiplet states in the  $(^3\text{He}, \alpha)$ .

Finally, there is a position resolution of the detectors on the focal plane lower than which incoming particles cannot be differentiated by the detector, but this is better than 0.1 mm [15], which is much smaller than the sum of the target effects for the experiments described in this work.

Overall, the resolutions were approximately 10 keV for the  $(d, p)$  and  $(p, d)$  reactions, and about 30 keV for the  $(^3\text{He}, \alpha)$  reaction.

# Bibliography

- [1] S.V. Szwec. Transfer reaction studies of medium mass nuclei - single-particle occupancies and neutrinoless double beta decay. *PhD Thesis*, University of Manchester, 2017.
- [2] M. Moser, P. Reichart, W. Carli, C. Greubel, K. Peeper, P. Hartung, and G. Dollinger. High brilliance multicusp ion source for hydrogen microscopy at SNAKE. *Nuclear Instruments and Methods in Physics Research B*, 273:226–230, February 2012.
- [3] R Hertenberger, A Metz, Y Eisermann, K El Abiary, A Ludewig, C Pertl, S Trieb, H-F Wirth, P Schiemenz, and G Graw. The stern–gerlach polarized ion source for the munich mp-tandem laboratory, a bright source for unpolarized hydrogen and helium ion beams as well. *Nuclear Instruments and Methods in Physics Research Section A: Accelerators, Spectrometers, Detectors and Associated Equipment*, 536(3):266–272, 2005.
- [4] M. Bacal and M. Wada. Negative hydrogen ion production mechanisms. *Applied Physics Reviews*, 2(2):021305, June 2015.
- [5] W. Assmann, H. Münzer, L. Rohrer, and S.J. Skorka. High voltage tests with the mp-tandem at munich. *Nuclear Instruments and Methods*, 137(1):19 – 21, 1976.
- [6] R. G. Herb. The pelletron accelerator. *IEEE Transactions on Nuclear Science*, 18(3):71–75, 1971.
- [7] E. Almqvist, C. Broude, M. A. Clark, J. A. Kuehner, and A. E. Litherland. Atomic charge states in carbon of 10-to 40-Mev ions; application to tandem accelerators. *Canadian Journal of Physics*, 40:954, January 1962.
- [8] J. C. Overley, P. D. Parker, and D. A. Bromley. The energy calibration of tandem accelerators. *Nuclear Instruments and Methods*, 68(1):61–69, January 1969.
- [9] William A Higinbotham and S Rankowitz. A combined current indicator and integrator. *Review of Scientific Instruments*, 22(9):688–690, 1951.

- [10] G. Dollinger and T. Faestermann. Physics at the Munich Tandem Accelerator Laboratory. *ArXiv e-prints*, February 2018.
- [11] HJ Scheerer, H Vonach, M Löffler, Avd Decken, M Goldschmidt, CA Wiedner, and HA Enge. The multipole element of the q3d spectrograph for correction of the kinematic broadening. *Nuclear Instruments and Methods*, 136(2):213–224, 1976.
- [12] M Goldschmidt, D Rieck, and CA Wiedner. Performance of the first qddd spectrograph. Technical report, 1972.
- [13] S. Gillespie. Indirect studies of astrophysical reaction rates through transfer reactions. *PhD Thesis*, University of York, 2016.
- [14] H.F. Wirth. *Maier-Leibnitz-Laboratorium Annual Report*. page 71, 2000.
- [15] Hans-Friedrich Wirth. *Bau eines hochauflösenden Fokalebenenendetektors für den Münchner Q3D-Magnetspektrographen*. Dissertation, Technische Universität München, München, 2001.
- [16] G.F. Knoll. *Radiation Detection and Measurement*. Wiley, 2000.
- [17] Kenneth S Krane. *Introductory nuclear physics*. Wiley, New York, NY, 1988.
- [18] DH Gloeckner, MH Macfarlane, and Steven C Pieper. Ptolemy, a program for heavy-ion direction-reaction calculations. Technical report, Argonne National Lab., 1976.
- [19] Ernest Rutherford. Lxxix. the scattering of  $\alpha$  and  $\beta$  particles by matter and the structure of the atom. *The London, Edinburgh, and Dublin Philosophical Magazine and Journal of Science*, 21(125):669–688, 1911.
- [20] TB Ryves. The effects of scatter in a proton recoil telescope. *Nuclear Instruments and Methods in Physics Research Section A: Accelerators, Spectrometers, Detectors and Associated Equipment*, 240(2):379–382, 1985.
- [21] W. K. Chu. Calculation of energy straggling for protons and helium ions. *Phys. Rev. A*, 13:2057–2060, Jun 1976.
- [22] Harald A. Enge. Magnetic spectrographs for nuclear reaction studies. *Nuclear Instruments and Methods*, 162(1):161–180, June 1979.